

Distribution-Free Online Change Detection for Low-Rank Images

Tingnan Gong¹, Seong-Hee Kim¹, and Yao Xie¹

¹H. Milton Stewart School of Industrial and Systems Engineering,, Georgia Institute of Technology

Abstract

We present a distribution-free CUSUM procedure designed for online change detection in a time series of low-rank images, particularly when the change causes a mean shift. We represent images as matrix data and allow for temporal dependence, in addition to inherent spatial dependence, before and after the change. The marginal distributions are assumed to be general, not limited to any specific parametric distribution. We propose new monitoring statistics that utilize the low-rank structure of the in-control mean matrix. Additionally, we study the properties of the proposed detection procedure, assessing whether the monitoring statistics effectively capture a mean shift and evaluating the rate of increase in average run length relative to the control limit in both in-control and out-of-control cases. The effectiveness of our procedure is demonstrated through simulated and real data experiments.

1. Introduction

In modern manufacturing, rapid improvements in sensor technology allow the industry to acquire data with much higher dimensions than decades ago. For example, images of layers in 3D printing [7] can be obtained approximately every five seconds. For monitoring purposes, the image data is usually translated into high-dimensional matrix data. However, online monitoring of this high-dimensional matrix data in practical scenarios faces multifaceted challenges:

- *Temporal independence*: Due to the high sampling rate, weak auto-correlation among consecutive images is nearly inevitable. Long-lasting auto-correlation is also common in specific industrial problems. For example, in the case of in-situ detection of laser power bed fusion (LPBF) [15], an anomaly called a hot spot may happen. When the laser beam repeatedly irradiates a thermally insulated region, heat builds up exceptionally quickly, leading to the formation of a hot spot. In the view of a thermographic camera, the pixels in the center of the overheating area remain hot (high intensity) while the edges slowly cool down, causing durable auto-correlation and non-stationary spatial correlation.

- *Spatial independence*: Individual components of a high-resolution matrix tend to exhibit weak spatial correlation, thus violating the assumption of spatial independence. As mentioned in the aforementioned in-situ detection problem of LPBF, the hot spot anomaly can lead to unusual spatial correlation.
- *Data normality*: Violations of normality in data can result in serious deviation from theoretical analyses and conclusions derived based on the normality assumption, as discussed in [50]. [9] tackle the normality issue by transforming low-dimensional vectors into nearly normally distributed data. However, this technique turns out to be computationally prohibitive in high dimensions.
- *High dimensionality*: High-dimensional matrix data can drastically increase the complexity of any practical algorithm designed for univariate data. Additionally, collinearity or rank deficiency presents a tricky nature of high-dimensional matrix data. Many techniques, including but not limited to principal components analysis (PCA) [12] and process projection and fusion [51], aim to simultaneously reduce dimensionality and improve computational efficiency.

One way to handle high-dimensional matrix data is to adopt the profile monitoring perspective, as in [44], [43] and [32]. Procedures that employ this approach make a compromise by treating the high-dimensional matrix data as a long vector of predictors, sacrificing the spatial data structure. Practitioners then construct the response in single or multiple channels and develop appropriate models to characterize the functional relationship between the response and the predictors. The parametric regression model serves as one of the primary instruments in profile monitoring for describing this functional relationship. [8], [53], [52] and [36] perform profile monitoring using linear regression models. [22], [42], and [35] introduce non-linear profile monitoring to enhance interpretability. Other profile monitoring works utilize dimension reduction techniques to extract features, such as PCA and independent component analysis (ICA). [11] discuss comparisons between regression-based and PCA-based profile monitoring procedures.

Another approach is to use wavelet-based distribution-free profile monitoring procedures [27, 40] for high-dimensional vectors. These methods can partially address the mentioned challenges, including general marginal distributions and high dimensionality. However, profile monitoring tends to alter the original matrix structure and results in a loss of spatial information. Additionally, none of the aforementioned works incorporate general temporal correlation.

To mitigate the loss of information caused by data structure transformation, some works exploit matrix characteristics directly and construct matrix-based monitoring procedures. [34] categorize various matrix-based monitoring procedures, including spatial and multivariate-matrix-analysis-based control charts.

Recent works either combine multiple popular techniques or develop new models on matrix data from images. Among the procedures that integrate multiple popular techniques, [47] employ low-rank tensor decomposition to achieve dimension reduction and feature extraction and monitor the extracted features using Hotelling T^2 and Q control charts. Their methodology does not strictly require data normality and independence. However, their Phase-I calibration of the control limits is time-consuming due to the estimation of the empirical distribution of statistics. [25] and [13]

utilize wavelet transformations on matrix data to extract features and then build control charts. [25] perform a generalized likelihood ratio (GLR) control chart on extracted features. [13] further extend the approach in [25] by combining it with a regression-based parametric model to accommodate underlying data correlation. However, they still require data normality. [1] compress data using partial least squares discriminant analysis and then construct the control statistics using Delaunay triangulation [26] to segment the squared error matrix into triangles, computing the area within each triangle as control statistics. Despite the novelty of this technique, the assumption of data independence limits its broad application. Region of interest (ROI) is a popular data compression technique for matrix processing. Based on this tool, [33] incorporate the GLR control chart to monitor the average intensity vector calculated from these regions, assuming the presence of at most one cluster of defects in the images. [20] extend this approach further to detect multiple clusters of defects in images. [3] consider the combination of ROIs and one-way analysis of variance (ANOVA).

On the other hand, there are procedures that develop new models on the matrices. For a series of images with a smooth background, [48] propose a smooth-sparse decomposition (SSD) model to decompose observations into the background and potential sparse anomalies. However, the SSD model cannot incorporate temporal information into the data. Building on this work, [49] extend the SSD methodology with a spatio-temporal smooth-sparse decomposition (ST-SSD) model to tackle both temporal information and spatial patterns.

Although initially not developed for matrix monitoring, some spatio-temporal monitoring charts [21, 29, 28] used in the environment and public health surveillance can be adapted for matrix monitoring. Another thread of research addresses specific matrix monitoring problems in the industry. One of the applications that has garnered significant attention is matrix monitoring in metal additive manufacturing [46, 10, 23, 30, 18].

In this paper, we propose the distribution-free low-rank image monitoring (DFLIM) procedure to perform online change detection for a time series of matrices. This work is closely related to [17], which considers a special case when the in-control mean image matrix has rank one. We extend the approach of [17] to the general case where the rank of the in-control mean image matrix can be higher than one but still low-rank. Our procedure’s monitoring statistics are constructed based on singular value decomposition (SVD) of the in-control mean matrix and projected observations. These statistics are then coupled with CUSUM recursion, which can be computed recursively online. We analyze the theoretical properties of the DFLIM procedure in terms of the in-control average run length (ARL_0) and out-of-control average run length (ARL_1). These metrics evaluate how frequently a false alarm occurs when a monitored process is in control and how fast a change can be detected when the process is out of control. Furthermore, we empirically study the capability of the procedure against temporal dependence and non-normality of the data. The effectiveness of the proposed procedure is demonstrated through simulated and real data experiments.

The remainder of the paper is organized as follows: Section 2 describes our problem and assumptions. Section 3 proposes the DFLIM procedure, which utilizes a CUSUM chart on T^2 statistics extracted from the high-dimensional matrix data. In Section 4, we conduct theoretical analysis on the mean shift size in our statistics and study the ARL behavior of the DFLIM procedure. In Section 5, we design simulated experiments designed to demonstrate the performance of the DFLIM

procedure and empirically support some claims that are challenging to prove analytically. Section 6 applies the DFLIM procedure to real data sets to demonstrate its broad applications, followed by concluding remarks in Section 7.

2. Problem Setup

At each time t , we observe a matrix denoted as $X_t \in \mathbb{R}^{p_1 \times p_2}$. At an unknown change point $k \in \{1, \dots, \infty\}$, the mean of X_t shifts from M_0 to M_1 . We can formulate the problem in terms of online hypothesis testing:

$$\begin{aligned} \text{H}_0 : X_t &= M_0 + \epsilon_t, \quad t = 1, 2, \dots \\ \text{H}_1 : X_t &= \begin{cases} M_0 + \epsilon_t, & t = 1, 2, \dots, k-1, \\ M_1 + \epsilon_t, & t = k, k+1, \dots \end{cases} \end{aligned} \quad (1)$$

where M_0 and M_1 are p_1 -by- p_2 matrices representing the in-control and out-of-control mean matrices, respectively. We assume that $p_1 \leq p_2$, which can always be achieved by transposing the image matrices if necessary. The noise matrix ϵ_t is assumed to have the same distribution across time t , whereas the parametric form of the distribution is unrestricted, allowing for temporal correlations between ϵ_t 's. We denote expectations before and after the change as $\mathbb{E}_0[\cdot]$ and $\mathbb{E}_1[\cdot]$, respectively. The covariance functions $\text{Cov}_0(\cdot)$ and $\text{Cov}_1(\cdot)$ are defined similarly.

Before the change, X_t follows marginal distribution F_0 with mean $\mathbb{E}_0[X_t] = M_0$, where we assume M_0 to be known. The assumption of known in-control mean matrix M_0 is reasonable in scenarios where a target mean pattern exists, such as in the production line of a printed circuit board (PCB) manufacturing process where the in-control pattern for a PCB is designed before production or when an adequate amount of in-control data is available to estimate the in-control process parameters accurately. Further discussion on this is provided in Section 3.2.

After the change (i.e., $t \geq k$), the observations X_t will exhibit a mean shift $\mathbb{E}_1[X_t] = M_1 = M_0 + A$, where $A \in \mathbb{R}^{p_1 \times p_2}$ represents the unknown non-zero mean shift. Throughout the paper, we assume that the following assumptions hold:

Assumption 1. *The marginal distributions of X_t for $t = 1, 2, \dots, k-1$ and $X_t - A$ for $t = k, k+1, \dots$ are F_0 .*

Assumption 2. *The in-control mean M_0 has a rank $r \ll \min\{p_1, p_2\}$, and its SVD is given as follows:*

$$M_0 = \sum_{i=1}^r \lambda_i u_i v_i^\top$$

where λ_i , u_i , and v_i represent the singular values, left singular vectors, and right singular vectors, respectively.

Assumption 1 implies that the shift affects the mean but that the distribution family and covariance structures remain unchanged after the shift. Assumption 2 ensures that the in-control mean M_0 has a low rank.

3. Distribution-Free Low-Rank Image Monitoring

Given the matrix data X_t , we extract two types of projections for detection statistics. First, using the left and right singular vectors, u_i and v_i , of the in-control mean M_0 , we compute the *first-type* projected observations $\beta_{i,t}$ for $i = 1, \dots, r$ as follows:

$$\beta_{i,t} = u_i^\top X_t v_i. \quad (2)$$

Next, we calculate the residual matrix in the form of $R_t = X_t - M_0$ and perform its SVD to obtain its singular values in descending order. We use the first $\min\{p_1, p_2\}$ singular values as the *second-type* projected observations $\gamma_{i,t}$ for $i = 1, \dots, \min\{p_1, p_2\}$.

The statistic consisting of both types of projected observations at time t is denoted as y_t :

$$y_t = [\beta_t^\top, \gamma_t^\top] = [\beta_{1,t}, \dots, \beta_{r,t}, \gamma_{1,t}, \dots, \gamma_{r,t}]^\top \in \mathbb{R}^{2r}, \quad (3)$$

where $\beta_t = [\beta_{1,t}, \dots, \beta_{r,t}]^\top$ and $\gamma_t = [\gamma_{1,t}, \dots, \gamma_{r,t}]^\top$. Note that $\beta_{i,t}$ is the projection of X_t onto the static directions u_i and v_i , whereas $\gamma_{i,t}$ represents the projection onto temporally varying directions, i.e., the singular vectors of R_t . We discuss why it is necessary to incorporate both types of projections into y_t in Section 4.

To establish a CUSUM procedure, we transform y_t into T^2 -type statistics T_t as follows:

$$T_t = (y_t - \mathbb{E}_0[y_t])^\top \text{Cov}_0^{-1}(y_t) (y_t - \mathbb{E}_0[y_t]), \quad (4)$$

which constitutes the primary component of the increment in the CUSUM statistics. Note that $\text{Cov}_0(y_t)$ refers to $\text{Cov}_0(y_t, y_t)$, which represents the covariance matrix of the vector y_t with itself. Throughout the paper, we use this abbreviated notation for the covariance matrix between the same vector.

The CUSUM statistics for the DFLIM procedure are defined recursively with $S_0 = 0$:

$$S_t = \max\{0, S_{t-1} + (T_t - \mathbb{E}_0[T_t] - c\sigma_T)\}, \quad t = 1, \dots, \quad (5)$$

where c is a pre-selected constant, and $\sigma_T > 0$ is the in-control marginal standard deviation of T_t (under the marginal distribution F_0). The DFLIM procedure stops and raises an out-of-control signal at time τ when the monitoring statistic exceeds a control limit $H > 0$:

$$\tau = \inf\{t > 0 : S_t \geq H\}. \quad (6)$$

Given the stopping time τ , we define $\text{ARL}_0 = \mathbb{E}_0[\tau]$ and $\text{ARL}_1 = \mathbb{E}_1[\tau]$. Here, ARL_0 represents the average time to raise a false alarm when the process is in-control, which is inversely proportional to the false alarm rate. ARL_1 measures how quickly a monitoring procedure can detect an anomaly when the process is initially out-of-control.

The detailed description of the DFLIM procedure is given in Algorithm 1.

Algorithm 1 Distribution-free Low-rank Image Monitoring

Input: Sequence of observations $\{X_t, t = 1, 2, \dots\}$, in-control mean matrix M_0 , in-control mean vector $\mathbb{E}_0[y_t]$, in-control covariance $\text{Cov}_0(y_t)$, constant c , standard deviation σ_T , and control limit H (whose determination is discussed in Section 3.1).

Output: stopping time τ .

- 1: Initialize $\tau = +\infty$, $t = 0$, and $S_0 = 0$.
 - 2: Perform SVD on M_0 to obtain directions u_i and v_i for projections with $i = 1, \dots, r$.
 - 3: **while** $S_t < H$ **do**
 - 4: Set $t = t + 1$ and obtain X_t .
 - 5: Compute $\beta_{i,t}$ for $i = 1, \dots, r$ as in (2).
 - 6: Obtain r largest singular values of $R_t = X_t - M_0$, i.e. $\gamma_{i,t}$ for $i = 1, \dots, r$.
 - 7: Form y_t as in (3) and compute T_t as in (4).
 - 8: Update the monitoring statistic S_t as in (5).
 - 9: **end while**
 - 10: Set $\tau = t$ and raise an out-of-control alarm.
-

3.1 Control limit determination and setup phase

In this section, we derive an expression for ARLs of the DFLIM procedure and explain how this expression can be used to determine the control limit H . Additionally, we explain how to estimate the parameters necessary for implementing the DFLIM procedure.

Without specifying the probability measure, we define the mean and variance parameters of T_t as follows:

$$m = \mathbb{E}[T_t], \quad \text{and} \quad \Omega^2 = \lim_{t \rightarrow \infty} t \text{Var} \left(\frac{\sum_{\ell=1}^t T_\ell}{t} \right),$$

where the expectation and the variance can be taken under either in-control or out-of-control phase. Here, Ω^2 represents the limiting variance parameter for T_t , which provides a better measure of process variability compared to marginal variance in the presence of temporal correlations. We can then define the standardized time-series of the first t observations $\{T_1, T_2, \dots, T_t\}$ as follows:

$$\mathcal{C}_t(s) \equiv \frac{\sum_{\ell=1}^{\lfloor ts \rfloor} T_\ell - tsm}{\sqrt{t\Omega^2}}, \quad s \in [0, 1].$$

In addition to Assumptions 1 and 2, we assume that $\{T_t : t = 1, 2, \dots\}$ satisfies the Functional Central Limit Theorem (FCLT):

Assumption 3 (FCLT). *Given $\{T_t : t = 1, 2, \dots\}$, the standardized time-series process $\mathcal{C}_t(\cdot)$ satisfies:*

$$\mathcal{C}_t(\cdot) \xrightarrow{\mathcal{D}} \mathcal{W}(\cdot) \quad \text{as } t \rightarrow \infty,$$

in the space $D[0, 1]$ where $\xrightarrow{\mathcal{D}}$ denotes convergence in distribution, $\mathcal{W}(\cdot)$ denotes a standard Brownian process, and the space $D[0, 1]$ contains functions defined on $[0, 1]$ that are right-continuous with left-hand limits.

For conditions under which the FCLT is applicable, one can refer to [16]. In Chapter 4.4 of [41], it is suggested that, in practical terms, it is generally justifiable to presume the validity of the FCLT when Ω^2 is finite.

Under the FCLT, [24] show that the limiting process of CUSUM statistics is closely related to a standard Brownian motion process, regardless of the parametric form of X_t , forming the basis for a distribution-free procedure. Furthermore, they derive an approximate expression of ARLs, including both ARL_0 and ARL_1 , based on the properties of the converged process of CUSUM statistics. The DFLIM procedure also achieves the distribution-free property under the FCLT and determines the control limit H using the approximate expression of ARLs of the converged process, as provided in Lemma 3.1. Similar results were reported in [4], however without a clear characterization of the process variability using Ω^2 .

Lemma 3.1 ([24]). *If $\{T_t : t = 1, 2, \dots\}$ satisfies Assumption 3, then*

$$\text{ARL} \approx \begin{cases} H^2/\Omega^2, & \text{if } d_T = 0, \\ \frac{\Omega^2}{2d_T^2} \left[\exp\left(-\frac{2Hd_T}{\Omega^2}\right) - 1 + \frac{2Hd_T}{\Omega^2} \right], & \text{otherwise,} \end{cases}$$

for large H , where $d_T = \mathbb{E}[T_t] - \mathbb{E}_0[T_t] - c\sigma_T$.

When the monitored process is in-control, we have $d_T = -c\sigma_T$. By plugging $d_T = -c\sigma_T$ in the ARL expression in Lemma 3.1 and setting it equal to a target ARL_0 , one can analytically solve for the value of the control limit H . As suggested in [39], a more accurate control limit H can be obtained by solving the following equation:

$$\text{ARL}_0 = \frac{\Omega_0^2}{2c\sigma_T^2} \left\{ \exp\left[\frac{2c\sigma_T(H + 1.166\Omega_0)}{\Omega_0^2}\right] - 1 - \frac{2c\sigma_T(H + 1.166\Omega_0)}{\Omega_0^2} \right\}, \quad (7)$$

where Ω_0^2 is the in-control Ω^2 . More details on the calculation of Ω_0^2 are in Appendix A. We summarize the calculation of parameters and the control limit H , along with other parameters required for the implementation of the DFLIM procedure, in Algorithm 2.

3.2 Additional parameter calibration

In this subsection, we discuss how to estimate M_0 when the target mean image is not well-defined and how to determine r from the estimated M_0 . Additionally, we provide a recommendation for choosing a constant c .

Estimation of M_0 . The estimation of M_0 is straightforward. With training in-control data X_1, \dots, X_n , a good estimator for M_0 is the sample average of in-control observations, namely $\widehat{M}_0 = \sum_{t=1}^n X_t/n$. Due to the Law of Large Numbers, \widehat{M}_0 approximates the true in-control mean matrix M_0 well when n is large.

Selection of r . The rank r of M_0 is obtained numerically using singular value hard thresholding [14]. Specifically, for the singular values of M_0 , denoted as $\lambda_1 \geq \dots \geq \lambda_{\min\{p_1, p_2\}}$, and given a threshold

Algorithm 2 Setup phase for the DFLIM procedure

Input: Sequence of in-control observations $\{X_t, t = 1, 2, \dots, n\}$, in-control mean matrix M_0 , rank r , constant c , and target ARL_0 .

Output: $\mathbb{E}_0[y_t]$, $\text{Cov}_0(y_t)$, σ_T , and H .

- 1: Perform SVD on M_0 to obtain directions u_i and v_i for projections with $i = 1, \dots, r$.
 - 2: **while** $t < n$ **do**
 - 3: Set $t = t + 1$ and obtain X_t .
 - 4: Compute $\beta_{i,t}$ for $i = 1, \dots, r$ as in (2).
 - 5: Obtain r largest singular values of $R_t = X_t - M_0$, i.e. $\gamma_{i,t}$ for $i = 1, \dots, r$.
 - 6: Form y_t as in (3).
 - 7: **end while**
 - 8: Approximate $\mathbb{E}_0[y_t]$ by $\bar{y} = 1/n \sum_{t=1}^n y_t$ and $\text{Cov}_0(y_t)$ by $1/(n-1) \sum_{t=1}^n (y_t - \bar{y})(y_t - \bar{y})^\top$.
 - 9: Compute T_t as in (4) for $t = 1, \dots, n$.
 - 10: Compute $\bar{T} = 1/n \sum_{t=1}^n T_t$.
 - 11: Approximate σ_T by $\sqrt{1/(n-1) \sum_{t=1}^n (\bar{T} - T_t)^2}$.
 - 12: Estimate variance parameter Ω_0^2 of T_t using the CvM estimator.
 - 13: Calculate control limit H by solving equation (7).
-

$\lambda > 0$, we find $r = \max\{i : \lambda_i \geq \lambda\}$. Alternatively, this threshold can be replaced by q where $r = \min\{i : \sum_{i'=1}^i \lambda_{i'}^2 / \sum_{i'=1}^{\min\{p_1, p_2\}} \lambda_{i'}^2 \geq q\}$. We use q because it is standardized in the interval $[0, 1]$, whereas λ is unbounded.

A commonly used rule-of-thumb is to choose $q = 0.9$ if the training size is sufficiently large. To avoid rejecting the null hypothesis H_0 in (1) too frequently (i.e., experiencing high false alarms) when the data is noisy and the training size is small, a small value of q can be chosen, resulting in a smaller r . Following the definitions in (2), we obtain

$$\widehat{M}_0 = \sum_{i=1}^{\min\{p_1, p_2\}} \hat{\lambda}_i \hat{u}_i \hat{v}_i^\top \quad \text{and} \quad \hat{\beta}_{i,t} = \hat{u}_i^\top X_t \hat{v}_i \quad \text{for } i = 1, \dots, r.$$

We also obtain $\hat{\gamma}_{i,t}$ for $i = 1, \dots, \min\{p_1, p_2\}$ as the singular values of $\widehat{R}_t = X_t - \widehat{M}_0$.

Selection of c . The constant c in (5) is related to the behavior of the ARL, according to the analysis in Section 4.3. It is preferable to choose a small, non-negative value of c so that $\mathbb{E}_0[d_T] < 0$ and $\mathbb{E}_1[d_T] > 0$ hold. [24] recommend that practitioners choose c within the range of 0.01 to 0.1 based on empirical studies.

4. Theoretical Analysis

In this section, we compute the expected difference between the in-control and out-of-control y_t . Then, we analyze the shift size in the expected values of the monitoring statistics T_t from the in-control to an out-of-control state. We also discuss the behaviors of ARL_0 and ARL_1 of the DFILM procedure.

4.1 Mean shift in y_t

For any fixed $i = 1, \dots, r$, it is straightforward to derive the in-control and out-of-control expectations of $\beta_{i,t}$:

$$\mathbb{E}_0[\beta_{i,t}] = u_i^\top \mathbb{E}_0[X_t]v_i = \lambda_i, \quad \mathbb{E}_1[\beta_{i,t}] = u_i^\top \mathbb{E}_1[X_t]v_i = \lambda_i + \alpha_i,$$

where α_i is defined as the static projection of the unknown shift A , namely

$$\alpha_i = u_i^\top A v_i, \quad i = 1, \dots, r. \quad (8)$$

Theorem 4.1 (Mean shift in $\beta_{i,t}$). *For any time t and index $i = 1, \dots, r$, the difference between the in-control and out-of-control expectations of $\beta_{i,t}$ is*

$$\mathbb{E}_1[\beta_{i,t}] - \mathbb{E}_0[\beta_{i,t}] = \alpha_i,$$

where α_i is defined in (8).

From Theorem 4.1, the statistic $\beta_{i,t}$ can capture the change, provided that the differences α_i are non-zero for some i . By the definition of α_i , if the singular value spaces of A and M_0 are similar, we can consider α_i as an approximation of the singular values of A . In such cases, constructing statistics aimed at detecting a shift in the expectation of $\beta_{i,t}$ can be effective. On the other hand, if the singular spaces of A and M_0 are nearly orthogonal, then α_i oscillates around zero, and $\beta_{i,t}$ cannot acutely reflect the change. Although these extreme cases are rare in practical applications, the potential risk that $\beta_{i,t}$ may not capture the change requires enhancing the robustness of the detection procedure by incorporating another statistic, $\gamma_{i,t}$.

To analyze the in-control and out-of-control properties of the statistic $\gamma_{i,t}$, We need the following two lemmas:

Lemma 4.2 ([5]). *For any time $t < k$, suppose R_t has independent and identically distributed (i.i.d.) entries with mean zero and variance σ^2 , and their fourth moments are finite. As $p_1, p_2 \rightarrow \infty, p_1/p_2 \rightarrow \eta \in (0, 1)$, we have:*

$$\sigma(1 - \sqrt{\eta}) \leq \lim_{p_1, p_2 \rightarrow \infty} \frac{\gamma_{i,t}}{\sqrt{p_2}} \leq \sigma(1 + \sqrt{\eta}), \quad i = 1, \dots, r, \text{ a.s.},$$

where $\gamma_{i,t}$ is the i th largest singular value of R_t .

Lemma 4.2 is a direct corollary from Theorem 2 in [5]. It provides asymptotic upper and lower bounds for the in-control $\gamma_{i,t}$. Specifically, the order of $\gamma_{i,t}$ is $\Theta(\sqrt{p_2})$. In the out-of-control case, the residual matrix can be decomposed into the shift matrix A and the zero-mean matrix $R_t - A$. Lemma 4.3 indicates that the asymptotic behavior of R_t is dominated by the deterministic limiting behavior of A , rather than the random matrix $R_t - A$.

Lemma 4.3 ([6]). *For $t \geq k$, suppose that $R_t - A$ have i.i.d. entries with zero mean and variance σ^2 , their fourth moments are finite, and the limit*

$$\lim_{p_1, p_2 \rightarrow \infty} p_1/p_2 = \eta > 0$$

exists. For $i = 1, \dots, r$, let ρ_i denote the i th largest singular value of A . Furthermore, assume

$$\lim_{p_1, p_2 \rightarrow \infty} \rho_i / \sqrt{p_1 p_2} = \bar{\rho}_i$$

exists and is distinct and strictly positive, satisfying $\bar{\rho}_1 > \dots > \bar{\rho}_r > 0$. Then $\gamma_{i,t}$ can be decomposed as

$$\gamma_{i,t} = \rho_i + z_i + m_i + \varepsilon_i, \quad i = 1, \dots, r \quad (9)$$

where z_i is a random variable dependent on the dimensions p_1 and p_2 with zero mean and bounded variance, ε_i is a random variable converging to zero in probability with respect to the dimensions p_1 and p_2 , and the deterministic term m_i satisfies

$$m_i = \frac{\sigma^2}{2} \left(\frac{\sqrt{\eta}}{\bar{\rho}_i^3 p_1 p_2} - \frac{1}{\sqrt{\eta} \bar{\rho}_i} \right).$$

Lemma 4.3 corresponds to Theorem 1.1 in [6], which decomposes the out-of-control $\gamma_{i,t}$ defined in (9) into several terms. The random noise ε_i vanishes as the dimensions grow, and z_i has zero mean. The deterministic term m_i diminishes with the dimensions p_1 and p_2 , converging to a constant of $-\sigma^2/(2\sqrt{\eta}\bar{\rho}_i)$. Given that the singular value of the underlying anomaly ρ_i is of the order $\Theta(\sqrt{p_1 p_2})$, it dominates the asymptotic behavior of $\gamma_{i,t}$.

Theorem 4.4 (Asymptotic mean shift in $\gamma_{i,t}$). *With the assumptions in Lemmas 4.2 and 4.3, the limit of the expected difference between in-control and out-of-control $\gamma_{i,t}$ is expressed as follows:*

$$\lim_{p_1, p_2 \rightarrow \infty} \frac{\mathbb{E}_1[\gamma_{i,t}] - \mathbb{E}_0[\gamma_{i,t}]}{\sqrt{p_1 p_2}} = \bar{\rho}_i.$$

The proof of the theorem is available in Appendix B. Asymptotically, the expectation of the singular values of R_t under an out-of-control state is dominated by the singular values of the shift A . Thus, incorporating γ_t into statistics enhances the robustness of the detection capability of the DFLIM procedure against the algebraic relationship between M_0 and A .

As mentioned in Theorem 4.1, if the left or right singular space of the shift A is orthogonal to $\text{span}(u_1, \dots, u_r)$ or $\text{span}(v_1, \dots, v_r)$, $\beta_{i,t}$ may not accurately reflect the shift, and $\gamma_{i,t}$ may help with detection. However, we choose not to rely solely on $\gamma_{i,t}$ for detection because β_t demonstrates stronger detection power when the shift A is close in shape to the in-control mean M_0 . Consider an extreme scenario where, for some non-zero constant c' , the equation $A = c'M_0$ holds. For large

dimensions p_1 and p_2 , Theorem 4.1, Lemma 4.2, and Lemma 4.3 imply

$$\begin{aligned}
& (\mathbb{E}_1[\beta_{i,t}] - \mathbb{E}_0[\beta_{i,t}]) - (\mathbb{E}_1[\gamma_{i,t}] - \mathbb{E}_0[\gamma_{i,t}]) \\
&= \alpha_i - \left(\rho_i + \frac{\sigma^2}{2} \left(\frac{\sqrt{\eta}}{\bar{\rho}_i^3 p_1 p_2} - \frac{1}{\sqrt{\eta} \bar{\rho}_i} \right) + \mathbb{E}_1[\varepsilon_i] - \mathbb{E}_0[\gamma_{i,t}] \right) \\
&= c' \lambda_i - \left(c' \lambda_i + \frac{\sigma^2}{2} \left(\frac{\sqrt{\eta}}{\bar{\rho}_i^3 p_1 p_2} - \frac{1}{\sqrt{\eta} \bar{\rho}_i} \right) + \mathbb{E}_1[\varepsilon_i] - \mathbb{E}_0[\gamma_{i,t}] \right) \\
&= \frac{\sigma^2}{2} \left(\frac{1}{\sqrt{\eta} \bar{\rho}_i} - \frac{\sqrt{\eta}}{\bar{\rho}_i^3 p_1 p_2} \right) - \mathbb{E}_1[\varepsilon_i] + \mathbb{E}_0[\gamma_{i,t}] \\
&\geq \sigma(1 - \sqrt{\eta})\sqrt{p_2} + o(\sqrt{p_2}) + \frac{\sigma^2}{2} \left(\frac{1}{\sqrt{\eta} \bar{\rho}_i} - \frac{\sqrt{\eta}}{\bar{\rho}_i^3 p_1 p_2} \right) - \mathbb{E}_1[\varepsilon_i]. \tag{10}
\end{aligned}$$

If we impose the assumption that for any dimensions p_1 and p_2 , the random variable ε_i is uniformly integrable, then the convergence of ε_i to zero in probability implies the convergence of the expectation of ε_i , namely $\mathbb{E}_1[\varepsilon_i] = o(1)$. On the right-hand side of inequality (10), if $\eta > 0$, the dominant term is $\sigma(1 - \sqrt{\eta})\sqrt{p_2}$, which grows to infinity with respect to dimensions p_1 and p_2 . In a special case where η is close to 1, the term $\sigma^2 (1/\sqrt{\eta} \bar{\rho}_i - \sqrt{\eta}/(\bar{\rho}_i^3 p_1 p_2)) / 2$ remains positive and still shows the advantage of the feature vector $\beta_{i,t}$ compared with $\gamma_{i,t}$. Therefore, for effective and robust detection, both statistics in y_t are necessary.

4.2 Beyond spatial independence: mean shift in T_t

We analyze the shift size in T_t when the assumption of spatial independence in Lemmas 4.2 and 4.3 is violated. The covariances $\text{Cov}(\gamma_{i,t}, \gamma_{j,t})$ and $\text{Cov}(\beta_{i,t}, \gamma_{j,t})$ remain unknown given that $\gamma_{i,t}$ are singular values of a (possibly non-central) random matrix. To conduct analysis, we define the in-control and out-of-control covariance matrices of y_t as follows:

$$\text{Cov}_0(y_t) = \Sigma = \begin{bmatrix} \Sigma_\beta & P \\ P^\top & \Sigma_\gamma \end{bmatrix}, \quad \text{Cov}_1(y_t) = \tilde{\Sigma} = \begin{bmatrix} \Sigma_\beta & \tilde{P} \\ \tilde{P}^\top & \tilde{\Sigma}_\gamma \end{bmatrix},$$

where

$$\Sigma_\beta = \text{Cov}_0(\beta_t), \quad P = \text{Cov}_0(\beta_t, \gamma_t), \quad \tilde{P} = \text{Cov}_1(\beta_t, \gamma_t), \quad \Sigma_\gamma = \text{Cov}_0(\gamma_t), \quad \text{and} \quad \tilde{\Sigma}_\gamma = \text{Cov}_1(\gamma_t).$$

It is evident that $\Sigma_\beta = \text{Cov}_1(\beta_t)$ when only a mean shift is assumed, as in a typical mean-shift detection problem. Corresponding to the block structures that differentiate β and γ , we also define the expected shift size in them as $\mathbb{E}_1[y_t] - \mathbb{E}_0[y_t] = \delta = [\delta_\beta^\top, \delta_\gamma^\top]^\top$.

Theorem 4.5. *The difference between the in-control and out-of-control expectations of the T_t statistics is expressed as follows:*

$$\mathbb{E}_1[T_t] - \mathbb{E}_0[T_t] = \Delta_1 + \Delta_2 + \Delta_3,$$

where

$$\begin{aligned}
\Delta_1 &= \text{tr} \left[(\Sigma/\Sigma_\beta)^{-1} \left(\tilde{\Sigma}/\Sigma_\beta \right) \right] - r, \\
\Delta_2 &= \text{tr} \left\{ (\Sigma/\Sigma_\beta)^{-1} \left[\Sigma_\beta^{-1/2} (P - \tilde{P}) \right]^\top \left[\Sigma_\beta^{-1/2} (P - \tilde{P}) \right] \right\}, \\
\Delta_3 &= \left\| \Sigma_\beta^{-1/2} \delta_\beta \right\|^2 + \left\| (\Sigma/\Sigma_\beta)^{-1/2} \left(P^\top \Sigma_\beta^{-1} \delta_\beta + \delta_\gamma \right) \right\|^2, \\
\Sigma/\Sigma_\beta &= \Sigma_\gamma - P^\top \Sigma_\beta^{-1} P, \quad \text{and} \quad \tilde{\Sigma}/\Sigma_\beta = \tilde{\Sigma}_\gamma - \tilde{P}^\top \Sigma_\beta^{-1} \tilde{P}.
\end{aligned}$$

The proof of the theorem is provided in Appendix B. According to Theorem 4.5, Δ_1 approximates to 0 when $\tilde{\Sigma}$ deviates slightly from Σ . In contrast, Δ_2 is positive because it is the trace of the multiplication of two positive definite matrices. The last term, Δ_3 , increases quadratically with the shift sizes in β_t and γ_t . Assuming non-zero shift sizes in β_t or γ_t , Δ_3 is also positive as validated by Theorems 4.1 and 4.4 under the assumption of independence among matrix entries. Overall, Theorem 4.5 demonstrates the approximate positivity of the mean shift in T_t , enabling DFLIM to raise an alarm after the change point quickly.

4.3 ARL₀ and ARL₁

In this section, we provide expressions of ARL₀ and ARL₁. Recall that ARL₀ and ARL₁ represent $\mathbb{E}_0[\tau]$ and $\mathbb{E}_1[\tau]$, respectively. According to Lemma 3.1, for the in-control case, we have:

$$\text{ARL}_0 = \mathbb{E}_0[\tau] \approx \frac{\Omega_0^2}{2(c\sigma_T)^2} \left[\exp\left(\frac{2c\sigma_T H}{\Omega_0^2}\right) - 1 - \frac{2c\sigma_T H}{\Omega_0^2} \right],$$

where ARL₀ increases exponentially with respect to the control limit H . For an out-of-control case, we obtain:

$$\text{ARL}_1 = \mathbb{E}_1[\tau] \approx \frac{\Omega_1^2}{2d_1^2} \left[\exp\left(-\frac{2Hd_1}{\Omega_1^2}\right) - 1 + \frac{2d_1 H}{\Omega_1^2} \right],$$

where Ω_1^2 represents Ω^2 under the out-of-control probability measure and $d_1 = \mathbb{E}_1[T_t] - \mathbb{E}_0[T_t] - c\sigma_T$. Given the approximate positivity of d_1 as validated in Theorem 4.5, ARL₁ increases on the order of $O(H)$ (i.e., increases linearly with respect to H). Consequently, for a large H , we have $\text{ARL}_1 \ll \text{ARL}_0$.

To study the behavior of ARL₁ when the assumption of unchanged Ω^2 is violated, we consider the case where the process variability shifts from Ω_0^2 to Ω_1^2 . Performing a Taylor expansion on $\mathbb{E}_1[\tau]$, we obtain

$$\begin{aligned}
\mathbb{E}_1[\tau] &\approx \frac{\Omega_1^2}{2d_1^2} \left[1 - \frac{2d_1 H}{\Omega_1^2} + \left(\frac{2d_1 H}{\Omega_1^2}\right)^2 + o\left(\frac{1}{\Omega_1^4}\right) - 1 + \frac{2d_1 H}{\Omega_1^2} \right] \\
&= \frac{2H^2}{\Omega_1^2} + o\left(\frac{1}{\Omega_1^2}\right).
\end{aligned}$$

This approximation illustrates that if $\Omega_1^2 > \Omega_0^2$, the detection of a shift becomes even faster compared to the case of unchanged Ω^2 . On the other hand, Ω_1^2 is smaller than Ω_0^2 , detection becomes slower. However, even with a decrease in Ω_1^2 , the reduction is typically not substantial compared to the

size of Ω_0^2 , which tends to be large in practice. Therefore, the slowdown in detection is usually not significant.

5. Simulated Experiments

In this section, we perform numerical experiments to compare the DFLIM procedure with existing procedures. Specifically, we consider the following three baselines: (1) MEWMA [38], which applies parallelized multivariate EWMA control charts to matrix data for efficient detection of local changes; (2) MGLR [37], which constructs monitoring statistics based on ROI and corresponding likelihood ratios; (3) ST-SSD [49], which decomposes the data into informative characteristics and noises.

5.1 Settings

First, we generate in-control matrices $\{X_t \in \mathbb{R}^{p_1 \times p_2} : t = 1, 2, \dots\}$ using the following equation:

$$X_t = M_0 + \sum_{j=0}^{\ell} \phi^j \varepsilon_{t-j}, \quad (11)$$

where M_0 is the low-rank in-control mean matrix, ε_t denote noise matrices, and $\phi > 0$ is the auto-correlation parameter. Equation (11) represents a moving average model of order ℓ . In our simulated experiments, we set $p_1 = 100$ and $p_2 = 200$. The in-control data are generated as follows:

- We vary the ranks of M_0 within the set $\{2, 5\}$. The rank-two M_0 is constructed as a chessboard with elements $M_0[j_1, j_2]$ for $j_1 = 1, 2, \dots, 100$ and $j_2 = 1, 2, \dots, 200$:

$$M_0[j_1, j_2] = \begin{cases} 0.1, & 10k_1 + 1 \leq j_1 \leq 10k_1 + 5, 40k_2 + 11 \leq j_2 \leq 40k_2 + 20, \\ 0.1, & 10k_1 + 6 \leq j_1 \leq 10k_1 + 10, 40k_2 + 21 \leq j_2 \leq 40k_2 + 30, \\ -0.1, & 10k_1 + 1 \leq j_1 \leq 10k_1 + 5, 40k_2 + 31 \leq j_2 \leq 40k_2 + 40, \\ -0.1, & 10k_1 + 6 \leq j_1 \leq 10k_1 + 10, 40k_2 + 1 \leq j_2 \leq 40k_2 + 10, \\ 0, & \text{otherwise,} \end{cases}$$

where $0 \leq k_1 \leq 4$ and $0 \leq k_2 \leq 9$. To extend the rank to five, we superimpose the rank-three approximation of the truncated first image of solar flare image data [45] onto the chessboard signal. Figure 1 displays the resulting images of the rank-two and rank-five M_0 .

- For the distribution of ε_t , we select one from the following two distributions:
 - (1) *Normal distribution*: We generate ε_t using the matrix normal distribution [19, Chapter 2].

Thus,

$$\varepsilon_t \stackrel{\text{i.i.d.}}{\sim} \mathcal{MN}(0, \Sigma_{\text{row}}, \Sigma_{\text{col}}), \quad (12)$$

where $\Sigma_{\text{row}} \in \mathbb{R}^{p_1 \times p_1}$ and $\Sigma_{\text{col}} \in \mathbb{R}^{p_2 \times p_2}$ are specified to capture the spatial correlations.

- (2) *Non-normal distribution:* We first generate $\tilde{\varepsilon}_t$ from (12) and then transform each entry $\tilde{\varepsilon}_t[j_1, j_2]$ into $\varepsilon_t[j_1, j_2]$ as follows:

$$\varepsilon_t[j_1, j_2] = -\log(1 - \Psi(\tilde{\varepsilon}_t[j_1, j_2])),$$

where $\Psi(\cdot)$ represents the cumulative distribution of the standard normal random variable. Thus, ε_t has entries $\varepsilon_t[j_1, j_2]$ that are exponentially distributed with an expectation of 1 and exhibit correlations among them.

- To incorporate spatial correlation, both covariance matrices Σ_{row} and Σ_{col} are specified using either tri-diagonal covariance or exponential covariance, defined as follows:

$$\text{Tri-diagonal} = \begin{bmatrix} 1 & \cdots & 0 & 0 \\ \vdots & \ddots & \vdots & \vdots \\ 0 & \cdots & 1 & 0.3 \\ 0 & \cdots & 0.3 & 1 \end{bmatrix}, \text{Exponential} = \begin{bmatrix} 1 & \cdots & 0.3^{p-2} & 0.3^{p-1} \\ \vdots & \ddots & \vdots & \vdots \\ 0.3^{p-2} & \cdots & 1 & 0.3 \\ 0.3^{p-1} & \cdots & 0.3 & 1 \end{bmatrix}, \quad (13)$$

where the dimensions of the covariance matrices vary in $\{p_1, p_2\}$, corresponding to the row and column sides.

- To incorporate auto-correlation, we vary the lag order $\ell \in \{5, 20\}$ for the moving average term $\sum_{j=0}^{\ell} \phi^j \varepsilon_{t-j}$ in (11), with the parameter ϕ fixed as $\phi = 0.5$.

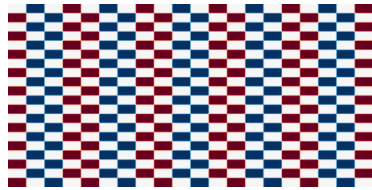
We generate the out-of-control matrices according to the following equation:

$$X_t = M_0 + A + \sum_{j=0}^{\ell} \phi^j \varepsilon_{t-j},$$

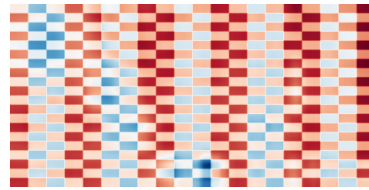
where the mean M_0 and the noise $\sum_{i=0}^{\ell} \phi^i \varepsilon_{t-i}$ follow the same settings as in the in-control matrices. We test the following four mean shifts for A :

- (i) Sparse:

$$A[j_1, j_2] = \begin{cases} 3, & \text{if } 8 \leq j_1 \leq 13 \text{ and } 18 \leq j_2 \leq 23, \\ 0, & \text{otherwise.} \end{cases}$$



(a) $\text{Rank}(M_0) = 2$



(b) $\text{Rank}(M_0) = 5$

Figure 1: In-control mean matrix M_0 with rank $r \in \{2, 5\}$.

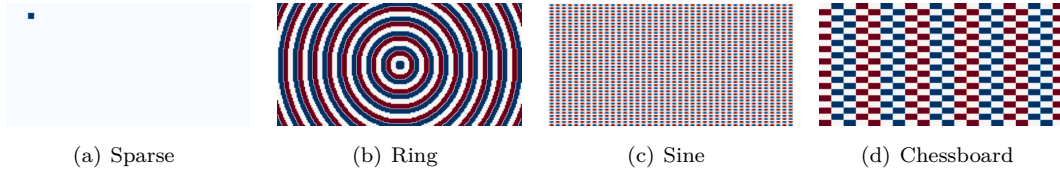


Figure 2: Four patterns of shift matrix A .

(ii) Ring:

$$A[j_1, j_2] = \begin{cases} 0.173, & \text{if } \lfloor \sqrt{(j_1 - 50)^2 + (j_2 - 100)^2} \rfloor = 12k_1 + k_2, \\ -0.173, & \text{if } \lfloor \sqrt{(j_1 - 50)^2 + (j_2 - 100)^2} \rfloor = 12k_1 + 8 + k_2, \\ 0, & \text{otherwise,} \end{cases}$$

where k_1 is some non-negative integer and $0 \leq k_2 \leq 3$.

(iii) Sine:

$$A[j_1, j_2] = 0.283 \sin \frac{j_2 \pi}{5} \sin \frac{2j_1 \pi}{5}.$$

(iv) Chessboard: identical to the rank-two M_0 .

The visual representation of the four shift patterns is provided in Figure 2.

5.2 In-control performance

In each in-control setting, we generate 1000 sequences, each consisting of 800 matrix observations. The target ARL_0 is set to 200. Baselines MEWMA, MGLR, and ST-SSD tune their control limits through trial-and-error using these 1000 sequences. For DFLIM, we set $c = 0.01$ for all experiments and determine the control limit by solving equation (7) for H . Each procedure is then applied to these 1000 sequences using its determined control limit to estimate ARL_0 .

In each in-control setting, we generate 1000 sequences, each consisting of 800 matrix observations. The target ARL_0 is set to 200. Baseline methods MEWMA, MGLR, and ST-SSD tune their control limits through trial-and-error using these 1000 sequences. For DFLIM, we determine the control limit by solving equation (7) for H . Subsequently, each procedure is applied to the same dataset to find the control limits.

Table 1 summarizes the control limits (H) and estimated ARL_0 values for different procedures. MEWMA, MGLR, and ST-SSD achieve ARL_0 values close to the target 200, as expected, because their control limits are determined through trial-and-error calibration using the same data sequences. The table also demonstrates that the analytically determined control limits for DFLIM provide relatively accurate ARL_0 values close to the target. The simulated data has complicated spatial correlations as defined in (13), and the target ARL_0 is set to a small value, potentially increasing the risk that the time horizon might not be long enough for the FCLT to be applicable. Despite these slight theoretical violations, the empirical ARL_0 values obtained for DFLIM are still quite accurate. These results suggest that (7) is widely applicable in practice.

Table 1: Control limit (H) and estimated ARL_0 for various settings of simulated processes with target $ARL_0 = 200$ (standard errors in parentheses).

Distribution	Rank	Lag	Covariance	MEWMA		MGLR		ST-SSD		DFLIM	
				H	ARL_0	H	ARL_0	H	ARL_0	H	ARL_0
Normal	2	5	Tri-diagonal	180.202	198.62 (6.248)	6.062	201.04 (5.495)	2.800	201.05 (5.680)	36.507	201.48 (5.321)
Normal	2	5	Exponential	180.219	200.41 (5.910)	6.043	200.72 (5.528)	2.799	199.42 (5.692)	36.654	197.26 (5.119)
Normal	2	20	Tri-diagonal	180.455	200.20 (5.866)	6.155	198.46 (5.465)	2.796	199.87 (6.036)	36.776	203.02 (5.188)
Normal	2	20	Exponential	180.415	198.12 (5.890)	6.236	200.17 (5.574)	2.804	200.17 (5.698)	36.935	200.81 (5.103)
Normal	5	5	Tri-diagonal	184.765	198.72 (8.941)	6.039	200.94 (5.694)	2.779	198.83 (5.576)	36.551	201.30 (5.297)
Normal	5	5	Exponential	183.968	201.29 (9.059)	6.015	198.83 (5.469)	2.796	201.10 (5.715)	36.688	201.28 (5.173)
Normal	5	20	Tri-diagonal	184.236	201.88 (9.081)	6.221	199.75 (5.640)	2.808	200.98 (5.687)	36.632	205.51 (5.354)
Normal	5	20	Exponential	184.509	198.50 (9.053)	6.203	200.92 (5.574)	2.783	198.36 (5.827)	36.641	197.76 (5.167)
Non-normal	2	5	Tri-diagonal	294.912	199.32 (10.903)	6.042	201.49 (5.562)	2.837	198.39 (5.935)	37.208	202.81 (5.167)
Non-normal	2	5	Exponential	296.649	201.74 (10.953)	6.013	200.26 (5.526)	2.814	200.38 (5.988)	37.416	200.32 (5.292)
Non-normal	2	20	Tri-diagonal	297.494	199.15 (10.911)	6.191	201.17 (5.839)	2.828	198.72 (5.883)	37.359	204.95 (5.187)
Non-normal	2	20	Exponential	299.497	200.49 (10.930)	6.173	198.74 (5.435)	2.834	200.51 (5.846)	37.510	202.34 (5.425)
Non-normal	5	5	Tri-diagonal	389.186	199.95 (10.926)	6.017	199.69 (5.446)	2.821	199.74 (5.596)	37.369	205.32 (5.383)
Non-normal	5	5	Exponential	391.227	199.95 (10.926)	5.988	200.12 (5.441)	2.832	199.70 (5.634)	37.283	206.09 (5.357)
Non-normal	5	20	Tri-diagonal	394.891	199.15 (10.911)	6.212	200.55 (5.578)	2.818	200.67 (5.817)	37.483	207.76 (5.351)
Non-normal	5	20	Exponential	394.642	199.95 (10.926)	6.215	201.63 (5.533)	2.834	200.08 (5.867)	37.565	206.17 (5.253)

5.3 Out-of-control performance

In out-of-control experiments, we consider shift matrix A with sparse, ring, sine, and chessboard patterns as described in Section 5.1, which are added to the in-control data. The experiment is repeated 1000 times for each procedure. The results of the out-of-control performances are summarized in Tables 2–5 for each shift pattern A .

The DFLIM procedure consistently outperforms the MEWMA and MGLR procedures across all shift patterns.

The MEWMA procedure detects shifts only in a few cases but with significant delay. MEWMA employs a profile monitoring technique, where the matrix is flattened into a long vector and segmented for separate handling. This approach risks losing spatial correlations due to flattening and segmentation. Another drawback is that each segment remains high-dimensional, making covariance estimation for each segment challenging. In our experiment, with 800 in-control data and segments of dimension 200, MEWMA’s performance suffers due to poor marginal covariance estimation across segments. Additionally, MEWMA assumes temporal independence, which is invalid in our complex auto-correlations experiments.

The MGLR procedure reduces data dimensionality by defining ROIs, but this process can result in local information loss within each ROI. Considering the nature of our shifts (sparse or alternating positive and negative), the mean of entries in each ROI tends to be close to zero. This cancellation of informative entries by taking the mean of each ROI in MGLR undermines its ability to detect a shift effectively.

The ST-SSD procedure is the most competitive baseline compared to DFLIM. In Table 2, DFLIM detects sparse shifts faster than ST-SSD, saving approximately 70 observations. Regarding the ring shift in Table 3, under normal noise distribution, DFLIM performs slightly worse than ST-SSD, with a lag of less than 10 observations. However, with non-normal noise distribution, ST-SSD outperforms DFLIM by approximately 20 observations, although both achieve significantly smaller ARL_1 values compared to MEWMA and MGLR. In Table 4, both DFLIM and ST-SSD detect the chessboard shift almost instantly, showing negligible differences between them. For the chessboard shift in Table

Table 2: Sparse shift: ARL_1 for various settings of simulated processes with target $ARL_0 = 200$ (standard errors in parentheses).

Distribution	Rank	Lag	Covariance	MEWMA	MGLR	ST-SSD	DFLIM
Normal	2	5	Tri-diagonal	198.93 (6.227)	207.34 (5.756)	79.17 (2.347)	15.06 (0.232)
Normal	2	5	Exponential	197.69 (6.249)	200.58 (5.425)	85.01 (2.603)	16.66 (0.289)
Normal	2	20	Tri-diagonal	196.08 (6.190)	188.46 (5.211)	80.64 (2.597)	15.61 (0.264)
Normal	2	20	Exponential	201.89 (6.215)	200.11 (5.618)	84.05 (2.600)	16.49 (0.278)
Normal	5	5	Tri-diagonal	180.50 (9.163)	202.62 (5.683)	74.58 (2.334)	14.77 (0.233)
Normal	5	5	Exponential	155.01 (8.373)	197.18 (5.409)	84.31 (2.661)	16.09 (0.271)
Normal	5	20	Tri-diagonal	153.96 (8.399)	198.62 (5.486)	83.17 (2.589)	15.18 (0.258)
Normal	5	20	Exponential	175.24 (8.724)	202.35 (5.428)	77.40 (2.417)	16.39 (0.275)
Non-normal	2	5	Tri-diagonal	156.04 (9.991)	197.86 (5.533)	83.06 (2.675)	20.52 (0.353)
Non-normal	2	5	Exponential	178.38 (10.501)	194.10 (5.516)	84.74 (2.624)	21.11 (0.387)
Non-normal	2	20	Tri-diagonal	163.70 (10.163)	191.24 (5.293)	82.38 (2.530)	21.03 (0.372)
Non-normal	2	20	Exponential	174.38 (10.415)	189.54 (5.334)	85.97 (2.708)	21.20 (0.388)
Non-normal	5	5	Tri-diagonal	164.00 (10.182)	202.14 (5.522)	85.50 (2.744)	21.03 (0.372)
Non-normal	5	5	Exponential	176.78 (10.467)	182.21 (5.268)	87.27 (2.784)	21.78 (0.396)
Non-normal	5	20	Tri-diagonal	182.37 (10.584)	195.56 (5.465)	80.65 (2.769)	20.80 (0.379)
Non-normal	5	20	Exponential	156.80 (10.011)	196.41 (5.581)	90.09 (2.824)	22.01 (0.397)

Table 3: Ring shift: ARL_1 for various settings of simulated processes with target $ARL_0 = 200$ (standard errors in parentheses).

Distribution	Rank	Lag	Covariance	MEWMA	MGLR	ST-SSD	DFLIM
Normal	2	5	Tri-diagonal	196.30 (6.062)	194.71 (5.712)	21.50 (0.687)	28.69 (0.498)
Normal	2	5	Exponential	197.92 (6.041)	209.54 (5.775)	23.73 (0.758)	27.41 (0.476)
Normal	2	20	Tri-diagonal	199.30 (6.110)	190.31 (5.435)	20.05 (0.610)	29.10 (0.490)
Normal	2	20	Exponential	197.52 (5.880)	198.82 (5.691)	24.04 (0.734)	26.81 (0.435)
Normal	5	5	Tri-diagonal	204.50 (9.416)	198.12 (5.554)	20.22 (0.579)	27.86 (0.461)
Normal	5	5	Exponential	159.62 (8.229)	194.84 (5.631)	24.05 (0.728)	26.20 (0.440)
Normal	5	20	Tri-diagonal	175.98 (8.595)	203.60 (5.518)	22.42 (0.661)	28.15 (0.490)
Normal	5	20	Exponential	184.53 (8.824)	195.35 (5.491)	24.35 (0.718)	27.19 (0.459)
Non-normal	2	5	Tri-diagonal	160.79 (10.106)	195.68 (5.555)	21.16 (0.648)	47.58 (0.929)
Non-normal	2	5	Exponential	193.44 (10.800)	208.74 (5.761)	24.00 (0.746)	40.47 (0.726)
Non-normal	2	20	Tri-diagonal	149.26 (9.814)	200.90 (5.598)	20.34 (0.626)	45.90 (0.869)
Non-normal	2	20	Exponential	181.07 (10.550)	193.64 (5.278)	23.34 (0.710)	42.59 (0.813)
Non-normal	5	5	Tri-diagonal	190.36 (10.744)	195.06 (5.407)	20.66 (0.633)	45.75 (0.852)
Non-normal	5	5	Exponential	192.76 (10.791)	185.25 (5.259)	25.85 (0.794)	39.06 (0.709)
Non-normal	5	20	Tri-diagonal	178.38 (10.501)	200.02 (5.537)	20.61 (0.639)	44.73 (0.869)
Non-normal	5	20	Exponential	191.16 (10.760)	190.57 (5.134)	26.90 (0.839)	41.36 (0.805)

Table 4: Sine shift: ARL_1 for various settings of simulated processes with target $ARL_0 = 200$ (standard errors in parentheses).

Distribution	Rank	Lag	Covariance	MEWMA	MGLR	ST-SSD	DFLIM
Normal	2	5	Tri-diagonal	201.12 (5.933)	199.93 (5.511)	31.12 (0.996)	5.29 (0.081)
Normal	2	5	Exponential	209.35 (6.448)	198.88 (5.576)	37.34 (1.169)	16.17 (0.244)
Normal	2	20	Tri-diagonal	191.17 (5.963)	187.88 (5.256)	32.41 (1.047)	5.54 (0.086)
Normal	2	20	Exponential	194.94 (6.011)	203.80 (5.514)	35.90 (1.062)	16.45 (0.263)
Normal	5	5	Tri-diagonal	210.28 (9.451)	192.23 (5.592)	29.65 (0.923)	5.45 (0.083)
Normal	5	5	Exponential	176.80 (8.450)	187.72 (5.215)	35.86 (1.076)	16.31 (0.273)
Normal	5	20	Tri-diagonal	172.29 (8.513)	203.99 (5.598)	30.92 (0.909)	5.54 (0.087)
Normal	5	20	Exponential	195.50 (9.001)	192.17 (5.401)	35.05 (1.029)	16.5 (0.266)
Non-normal	2	5	Tri-diagonal	156.80 (10.011)	205.74 (5.920)	35.32 (1.079)	6.50 (0.097)
Non-normal	2	5	Exponential	192.28 (10.775)	197.62 (5.561)	37.04 (1.116)	16.87 (0.255)
Non-normal	2	20	Tri-diagonal	165.11 (10.197)	184.36 (5.086)	35.08 (1.060)	6.59 (0.098)
Non-normal	2	20	Exponential	170.39 (10.327)	186.27 (5.357)	39.12 (1.249)	16.68 (0.254)
Non-normal	5	5	Tri-diagonal	183.17 (10.600)	198.31 (5.558)	33.06 (0.970)	6.60 (0.096)
Non-normal	5	5	Exponential	209.54 (11.097)	187.94 (5.486)	40.92 (1.226)	17.27 (0.266)
Non-normal	5	20	Tri-diagonal	218.33 (11.243)	193.34 (5.370)	34.40 (1.094)	6.40 (0.100)
Non-normal	5	20	Exponential	169.59 (10.309)	203.86 (5.566)	39.21 (1.262)	16.41 (0.260)

Table 5: Chessboard shift: ARL_1 for various settings of simulated processes with target $ARL_0 = 200$ (standard errors in parentheses).

Distribution	Rank	Lag	Covariance	MEWMA	MGLR	ST-SSD	DFLIM
Normal	2	5	Tri-diagonal	190.65 (6.146)	205.80 (5.895)	1.54 (0.030)	1.70 (0.017)
Normal	2	5	Exponential	193.27 (6.081)	207.11 (5.744)	1.78 (0.044)	1.97 (0.018)
Normal	2	20	Tri-diagonal	186.63 (6.145)	184.59 (4.887)	1.52 (0.031)	1.69 (0.017)
Normal	2	20	Exponential	199.48 (6.307)	199.14 (5.624)	1.74 (0.037)	1.97 (0.018)
Normal	5	5	Tri-diagonal	163.28 (8.942)	203.00 (5.583)	1.49 (0.030)	2.28 (0.021)
Normal	5	5	Exponential	135.63 (7.913)	199.87 (5.557)	1.76 (0.039)	2.62 (0.024)
Normal	5	20	Tri-diagonal	133.09 (7.833)	192.75 (5.604)	1.54 (0.031)	2.28 (0.021)
Normal	5	20	Exponential	146.96 (8.206)	198.12 (5.508)	1.77 (0.041)	2.59 (0.025)
Non-normal	2	5	Tri-diagonal	162.08 (10.129)	207.74 (5.870)	1.56 (0.030)	2.47 (0.023)
Non-normal	2	5	Exponential	171.71 (10.349)	196.14 (5.447)	1.75 (0.036)	2.77 (0.026)
Non-normal	2	20	Tri-diagonal	131.17 (9.328)	197.06 (5.611)	1.57 (0.031)	2.53 (0.023)
Non-normal	2	20	Exponential	157.46 (10.022)	195.98 (5.507)	1.91 (0.047)	2.80 (0.028)
Non-normal	5	5	Tri-diagonal	160.00 (10.088)	195.82 (5.581)	1.58 (0.031)	2.52 (0.024)
Non-normal	5	5	Exponential	169.59 (10.309)	192.56 (5.322)	1.82 (0.042)	2.85 (0.029)
Non-normal	5	20	Tri-diagonal	151.21 (9.872)	199.70 (5.491)	1.53 (0.032)	2.55 (0.025)
Non-normal	5	20	Exponential	145.62 (9.728)	200.69 (5.775)	1.86 (0.043)	2.86 (0.030)

5, both DFLIM and ST-SSD procedures detect the shift nearly instantly, with a negligible difference between them.

The ST-SSD procedure employs a regression framework to decompose observations into three components: the in-control mean matrix M_0 , the shift A , and the noise. Except for the sparse shift, ST-SSD achieves this decomposition effectively, resulting in successful detection. DFLIM incorporates static and dynamic statistics to construct monitoring statistics for change detection. In scenarios where a shift is algebraically similar to the in-control mean matrix, static features play a significant role in change detection, as seen in the chessboard shift of Figure 2(d). On the other hand, dynamic features dominate when a shift is algebraically different from the in-control mean matrix, as demonstrated in the sparse, ring, and sine shifts of Figures 2(a)-2(c). Hence, DFLIM robustly and efficiently detects changes across various settings.

As stated in Theorem 4.1, the first-type features $\beta_{i,t}$ consistently help achieve change detection when M_0 and M_1 are algebraically similar. This is empirically supported by the effectiveness of DFLIM in detecting the chessboard shift, which resembles the in-control mean. On the other hand, the effectiveness of the second-type features $\gamma_{i,t}$ becomes evident when dealing with large matrix dimensions, approaching the asymptotic theory outlined in Theorem 4.4. Experimental results show that normally distributed noises often lead to smaller ARL_1 compared to non-normal noises, likely due to slower convergence to the asymptotic theory associated with non-normal noises.

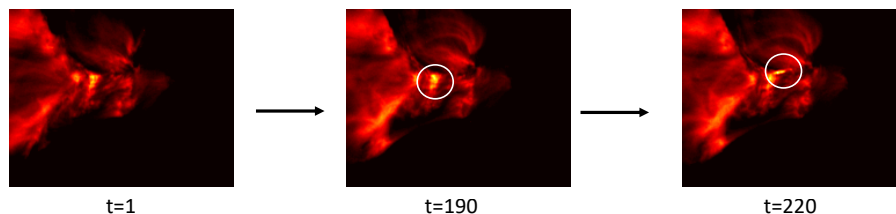


Figure 3: Solar flare images at $t = 1, 190, 220$. The white circles mark outbursts.

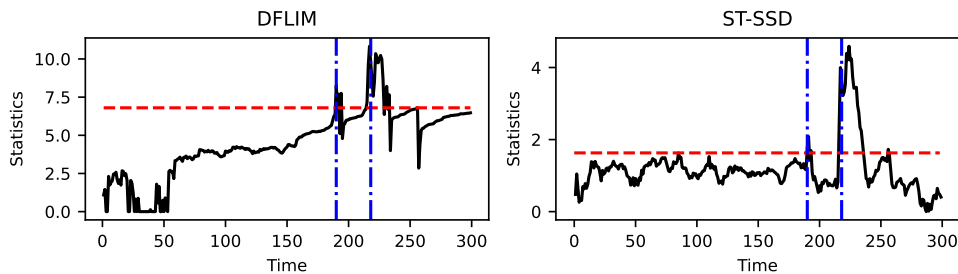


Figure 4: The monitoring process of DFLIM and ST-SSD on the solar flare images. Two outbursts occur around times 190 and 220, respectively, marked by vertical blue dashed lines. In each procedure, the control limit is indicated by a red dashed line, with the monitoring statistics shown in black.

6. Real Data Experiments

In this section, we apply DFLIM to real datasets to illustrate its broad applicability. More specifically, we analyze solar flare images in Section 6.1 and stochastic textured surface images in Section 6.2. We compare DFLIM with ST-SSD, excluding MEWMA and MGLR, because their control limits cannot be determined with a single in-control sequence.

We determine the control limit of DFLIM analytically by solving equation (7) for H . For ST-SSD, we determine its control limit using an empirical $(1 - 1/\text{ARL}_0)$ quantile estimate of the in-control monitoring statistics [49, Section 5.2].

6.1 Solar flare outburst

In this example, we aim to detect solar flare outbursts. Figure 3 shows solar flare images at times $t = 1, 190, 220$. The solar flare outbursts are represented by the bright spots in the images, indicated by the white circles. Prior knowledge indicates that two outbursts happen around times 190 and 220, respectively. The first outburst around time 190 is relatively moderate, while the second one around time 220 is more intense. The sequence consists of 300 images, each represented by a 232-by-292 matrix. We use the first 150 matrices as the training dataset and then perform monitoring on the entire sequence.

Detecting solar flare outbursts presents several challenges. First, each image is high-dimensional, containing nearly 70,000 pixels. Second, the low-rank property is not inherently applicable to solar flare images. To address this issue, we employ a patch technique that breaks the data into *patches* to promote the low-rank structure [31]. Each patched image exhibits a numerical rank of 10. Third, the dynamics of the changes are complex due to multiple change points and slowly evolving backgrounds. Specifically, many time points around 190 and 220 experience outbursts. To handle these multiple outbursts, we restart monitoring once an alarm is raised. Additionally, the changes in the data involve not only intense outbursts but also slow shifts in the background. To address the dynamic background, we process the data by taking consecutive differences of the images after the patch technique is performed, and we set the target $\text{ARL}_0 = 50,000$.

Figure 4 shows the results of ST-SSD and DFLIM to the solar flare images. ST-SSD effectively detects both moderate and intense outbursts without triggering false alarms. However, we observe that the monitoring statistic of ST-SSD is very close to its control limit around $t = 70, 80, 100$, corresponding to periods of normal solar flare activity. DFLIM demonstrates superior performance compared to ST-SSD, effectively identifying the outbursts around $t = 190$ and $t = 220$ with the detection statistics away from control limits prior to $t = 190$.

6.2 Stochastic textured surface monitoring

The online monitoring of additive manufacturing processes, commonly referred to as 3D printing, has drawn increasing attention due to its potential to reduce material waste. This example involves monitoring the production process of a parallelepiped ($20 \times 20 \times 20$ mm) using fused filament fabrication.

[7] use data from a sequential process to print two parallelepipeds. We use the same dataset and, refer to them as Build 1 (representing the process of building the first parallelepiped) and Build 2 (representing the process of building the second parallelepiped) hereafter. Build 1 is in control, while defects are intentionally introduced into Build 2 in the middle of the printing process.

During the printing process, layerwise images are captured by a video-imaging system installed above the printing area. To optimize bonding between consecutive layers, it is recommended to rotate the material extrusion direction iteratively. Consequently, the captured images are categorized into two types based on bead orientations: 45° and 135° . Each build consists of two sequences labeled as 45° and 135° , respectively, and these sequences are treated separately. Despite both sequences originating from the same build process, some images are occasionally skipped and not captured. Therefore, the index t in this example corresponds to the index of captured images and does not directly translate into time. The sequence with bead orientation 45° (135°) consists of 84 (81) images. For Build 1 (Build 2), the sequence ends at $t = 42$ ($t = 41$), after which defects are introduced at $t = 63$ ($t = 60$). Each image is represented as a 250-by-250 matrix. During monitoring, we utilize images from Build 1 to set up control limits and implementation parameters, then apply DFLIM and ST-SSD to the entire images.

Unlike the solar flare images, we do not need the patch technique for this dataset because the in-control data naturally exhibits low-rank properties due to the aligned paths of material extrusions.

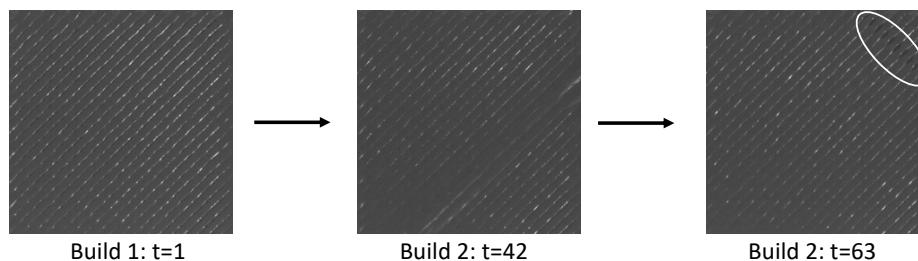


Figure 5: The material extrusion process is depicted at $t = 1, 42, 63$. At $t = 42$, there is a transition from the first to the second build. The bead orientation is 45° , and the white ellipse marks a defect.

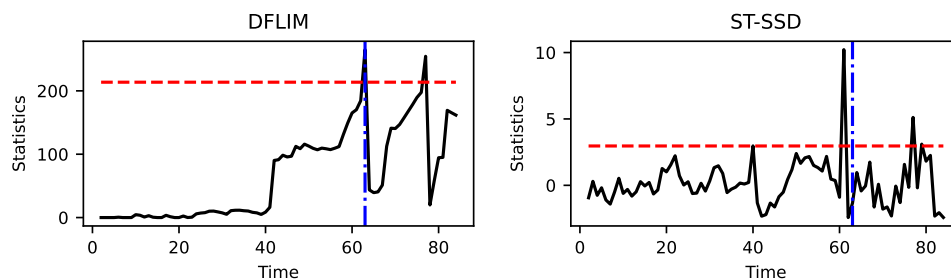


Figure 6: The monitoring process of DFLIM and ST-SSD on the 3D printing textured surface images with bead orientation at 45° . A build-to-build transition happens at $t = 42$, while a defect is introduced at $t = 63$, marked by vertical blue dashed lines in both figures. In each procedure, the control limit is indicated by a red dashed line, with the monitoring statistics shown in black.

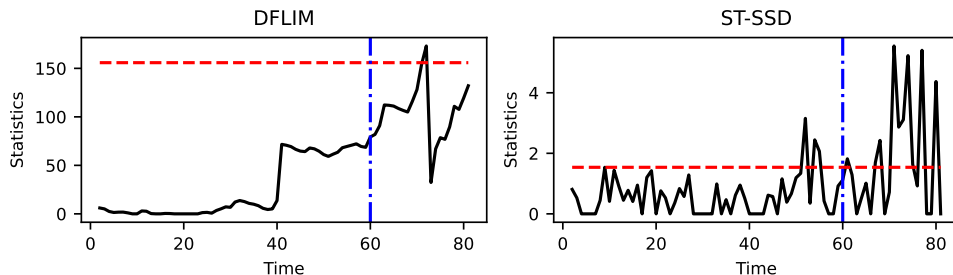


Figure 7: The monitoring process of DFLIM and ST-SSD on the 3D printing textured surface images with bead orientation at 135° . A build-to-build transition happens at $t = 41$, while a defect is introduced at $t = 60$, marked by vertical blue dashed lines in both figures. In each procedure, the control limit is indicated by a red dashed line, with the monitoring statistics shown in black.

However, this dataset presents challenges similar to those in the solar flare images, including high dimensionality and evolving backgrounds. Additionally, two more challenges arise with this dataset. First, the training sample size is small, consisting of only about 40 images. Second, the dataset exhibits build-to-build variability, which stems from dynamic factors in the printing area, such as changing illumination conditions during transitions between builds. Technically, the shift between builds could be considered a change point, but it is undesirable to detect this inter-build shift. Instead, we aim to detect a shift caused by actual defects, but the build-to-build variability increases the risk of false alarms.

For monitoring, we still take consecutive differences of images and restart the process upon detecting a change point. We set $ARL_0 = 4000$ for both bead orientations, suggesting approximately half a month between consecutive printer overhauls. Figure 6 displays the monitoring process for bead orientation 45° while Figure 7 shows the case for bead orientation 135° . In both cases, ST-SSD detects the change at the true change point but raises false alarms. DFLIM immediately detects the defect without raising a false alarm at the build-to-build transition in Figure 6. DFLIM still detects the defect in Figure 7 but has a delay of 12 images, roughly equivalent to one minute in real time (without considering skipped images).

7. Conclusion

In this paper, we propose a distribution-free monitoring procedure named DFLIM that can address the challenges posed by modern image data, including complex spatial-temporal dependence, non-normality, and high dimensionality with low-dimensional structure. We provide a comprehensive theoretical discussion on the detection ability and the behavior of ARL_0 and ARL_1 for the proposed procedure under reasonable assumptions. Extensive simulations are conducted using various distributions, ranks, and spatial-temporal correlation structures to validate the generality of DFLIM. Additionally, we apply DFLIM to two real datasets, solar flare datasets and additive manufacturing datasets, to demonstrate its applicability to real-world scenarios.

Acknowledgement

This work is partially supported by an NSF CAREER CCF-1650913, NSF DMS-2134037, CMMI-2015787, CMMI-2112533, DMS-1938106, DMS-1830210, and the Coca-Cola Foundation.

References

- [1] Adel Alaeddini, Abed Motasemi, and Syed Hasib Akhter Faruqui. A spatiotemporal outlier detection method based on partial least squares discriminant analysis and area delaunay triangulation for image-based process monitoring. *IISE Transactions*, 50(2):74–87, 2018.
- [2] Christos Alexopoulos, Nilay Tamk Argon, David Goldsman, Gamze Tokol, and James R Wilson. Overlapping variance estimators for simulation. *Operations Research*, 55(6):1090–1103, 2007.
- [3] Farzad Amirkhani and Amirhossein Amiri. A novel framework for spatiotemporal monitoring and post-signal diagnosis of processes with image data. *Quality and Reliability Engineering International*, 36(2):705–735, 2020.
- [4] Michael Bagshaw and Richard A Johnson. The effect of serial correlation on the performance of CUSUM tests II. *Technometrics*, 17(1):73–80, 1975.
- [5] Zhi-Dong Bai and Yong-Qua Yin. Limit of the smallest eigenvalue of a large dimensional sample covariance matrix. *The Annals of Probability*, 21(3):1275 – 1294, 1993.
- [6] Włodek Bryc and Jack W Silverstein. Singular values of large non-central random matrices. *Random Matrices: Theory and Applications*, 9(04):2050012, 2020.
- [7] Fabio Caltanissetta, Luisa Bertoli, and Bianca Maria Colosimo. In-situ monitoring of image texturing via random forests and clustering with applications to additive manufacturing. *IISE Transactions*, 0(0):1–15, 2023.
- [8] Tee-Chin Chang and Fah-Fatt Gan. Monitoring linearity of measurement gauges. *Journal of Statistical Computation and Simulation*, 76(10):889–911, 2006.
- [9] Youn-Min Chou, Alan M Polansky, and Robert L Mason. Transforming non-normal data to normality in statistical process control. *Journal of Quality Technology*, 30(2):133–141, 1998.
- [10] Bianca M Colosimo and Marco Grasso. Spatially weighted PCA for monitoring video image data with application to additive manufacturing. *Journal of Quality Technology*, 50(4):391–417, 2018.
- [11] Bianca M Colosimo and Massimo Pacella. A comparison study of control charts for statistical monitoring of functional data. *International Journal of Production Research*, 48(6):1575–1601, 2010.

- [12] Bart De Ketelaere, Mia Hubert, and Eric Schmitt. Overview of PCA-based statistical process-monitoring methods for time-dependent, high-dimensional data. *Journal of Quality Technology*, 47(4):318–335, 2015.
- [13] Dariush Eslami, Hamidreza Izadbakhsh, Orod Ahmadi, and Marzieh Zarinbal. Spatial-nonparametric regression: an approach for monitoring image data. *Communications in Statistics - Theory and Methods*, 0(0):1–24, 2021.
- [14] Matan Gavish and David L Donoho. Optimal shrinkage of singular values. *IEEE Transactions on Information Theory*, 63(4):2137–2152, 2017.
- [15] Ian Gibson, David W Rosen, Brent Stucker, Mahyar Khorasani, David Rosen, Brent Stucker, and Mahyar Khorasani. *Additive Manufacturing Technologies*, volume 17. Springer, 2021.
- [16] Peter W Glynn and Donald L Iglehart. Large-sample theory for standardized time series: an overview. In *Proceedings of the 17th Conference on Winter Simulation*, pages 129–134, 1985.
- [17] Tingnan Gong, Di Liu, Heeseon Kim, Seong-Hee Kim, Taeheung Kim, Dongki Lee, and Yao Xie. Distribution-free image monitoring with application to battery coating process. *IIEE Transactions*, 0(0):1–14, 2024.
- [18] Shenghan Guo, Weihong ”Grace” Guo, and Linkan Bain. Hierarchical spatial-temporal modeling and monitoring of melt pool evolution in laser-based additive manufacturing. *IIEE Transactions*, 52(9):977–997, 2020.
- [19] Arjun K Gupta and Daya K Nagar. *Matrix Variate Distributions*. Chapman and Hall/CRC, 2018.
- [20] Zhen He, Ling Zuo, Min Zhang, and Fadel M Megahed. An image-based multivariate generalized likelihood ratio control chart for detecting and diagnosing multiple faults in manufactured products. *International Journal of Production Research*, 54(6):1771–1784, 2016.
- [21] Wei Jiang, Sung Won Han, Kwok-Leung Tsui, and William H Woodall. Spatiotemporal surveillance methods in the presence of spatial correlation. *Statistics in Medicine*, 30(5):569–583, 2011.
- [22] RB Kazemzadeh, R Noorossana, and A Amiri. Monitoring polynomial profiles in quality control applications. *The International Journal of Advanced Manufacturing Technology*, 42(7):703–712, 2009.
- [23] Mojtaba Khanzadeh, Sudipta Chowdhury, Mark A Tschopp, Haley R Doude, Mohammad Maruffuzzaman, and Linkan Bian. In-situ monitoring of melt pool images for porosity prediction in directed energy deposition processes. *IIEE Transactions*, 51(5):437–455, 2019.
- [24] Seong-Hee Kim, Christos Alexopoulos, Kwok-Leung Tsui, and James R Wilson. A distribution-free tabular CUSUM chart for autocorrelated data. *IIE Transactions*, 39(3):317–330, 2007.

- [25] Mehdi Koosha, Rassoul Noorossana, and Fadel Megahed. Statistical process monitoring via image data using wavelets. *Quality and Reliability Engineering International*, 33(8):2059–2073, 2017.
- [26] Der-Tsai Lee and Bruce J Schachter. Two algorithms for constructing a delaunay triangulation. *International Journal of Computer & Information Sciences*, 9(3):219–242, 1980.
- [27] Joongsup Lee, Youngmi Hur, Seong-Hee Kim, and James R Wilson. Monitoring nonlinear profiles using a wavelet-based distribution-free CUSUM chart. *International Journal of Production Research*, 50(22):6574–6594, 2012.
- [28] Mi Lim Lee, David Goldsman, and Seong-Hee Kim. Robust distribution-free multivariate CUSUM charts for spatiotemporal biosurveillance in the presence of spatial correlation. *IIE Transactions on Healthcare Systems Engineering*, 5(2):74–88, 2015.
- [29] Mi Lim Lee, David Goldsman, Seong-Hee Kim, and Kwok-Leung Tsui. Spatiotemporal biosurveillance with spatial clusters: control limit approximation and impact of spatial correlation. *IIE Transactions*, 46(8):813–827, 2014.
- [30] Chenang Liu, Zhenyu Kong, Suresh Babu, Chase Joslin, and James Ferguson. An integrated manifold learning approach for high-dimensional data feature extractions and its applications to online process monitoring of additive manufacturing. *IISE Transactions*, 53(11):1215–1230, 2021.
- [31] David G Lowe. Object recognition from local scale-invariant features. In *Proceedings of the seventh IEEE international conference on computer vision*, volume 2, pages 1150–1157. Ieee, 1999.
- [32] Mohammad Reza Maleki, Amirhossein Amiri, and Philippe Castagliola. An overview on recent profile monitoring papers (2008–2018) based on conceptual classification scheme. *Computers & Industrial Engineering*, 126:705–728, 2018.
- [33] Fadel M Megahed, Lee J Wells, Jaime A Camelio, and William H Woodall. A spatiotemporal method for the monitoring of image data. *Quality and Reliability Engineering International*, 28(8):967–980, 2012.
- [34] Fadel M Megahed, William H Woodall, and Jaime A Camelio. A review and perspective on control charting with image data. *Journal of Quality Technology*, 43(2):83–98, 2011.
- [35] Javier M Moguerza, Alberto Muñoz, and Stelios Psarakis. Monitoring nonlinear profiles using support vector machines. In *Iberoamerican congress on pattern recognition*, pages 574–583. Springer, 2007.
- [36] R Noorossana, A Amiri, Sa Vaghefi, and E Roghanian. Monitoring process performance using linear profiles. In *Proceedings of the 3rd International Industrial Engineering Conference, Tehran, Iran*, 2004.

- [37] Yarema Okhrin, Wolfgang Schmid, and Ivan Semeniuk. New approaches for monitoring image data. *IEEE Transactions on Image Processing*, 30:921–933, 2021.
- [38] Philipp Otto. Parallelized monitoring of dependent spatiotemporal processes. In *Frontiers in Statistical Quality Control 13*, pages 165–183. Springer, 2021.
- [39] David Siegmund. *Sequential Analysis: Tests and Confidence Intervals*. Springer Science & Business Media, 1985.
- [40] Huizhu Wang, Seong-Hee Kim, Xiaoming Huo, Youngmi Hur, and James R Wilson. Monitoring nonlinear profiles adaptively with a wavelet-based distribution-free CUSUM chart. *International Journal of Production Research*, 53(15):4648–4667, 2015.
- [41] Ward Whitt. Stochastic-process limits: an introduction to stochastic-process limits and their application to queues. *Space*, 500:391–426, 2002.
- [42] JD Williams, Jeffrey B Birch, William H Woodall, and Nancy M Ferry. Statistical monitoring of heteroscedastic dose-response profiles from high-throughput screening. *Journal of Agricultural, Biological, and Environmental Statistics*, 12(2):216–235, 2007.
- [43] William H Woodall. Current research on profile monitoring. *Production*, 17:420–425, 2007.
- [44] William H Woodall, Dan J Spitzner, Douglas C Montgomery, and Shilpa Gupta. Using control charts to monitor process and product quality profiles. *Journal of Quality Technology*, 36(3):309–320, 2004.
- [45] Yao Xie, Jiaji Huang, and Rebecca Willett. Change-point detection for high-dimensional time series with missing data. *IEEE Journal of Selected Topics in Signal Processing*, 7(1):12–27, 2012.
- [46] Hao Yan, Marco Grasso, Kamran Paynabar, and Bianca Maria Colosimo. Real-time detection of clustered events in video-imaging data with applications to additive manufacturing. *IIEE Transactions*, 54(5):464–480, 2022.
- [47] Hao Yan, Kamran Paynabar, and Jianjun Shi. Image-based process monitoring using low-rank tensor decomposition. *IEEE Transactions on Automation Science and Engineering*, 12(1):216–227, 2014.
- [48] Hao Yan, Kamran Paynabar, and Jianjun Shi. Anomaly detection in images with smooth background via smooth-sparse decomposition. *Technometrics*, 59(1):102–114, 2017.
- [49] Hao Yan, Kamran Paynabar, and Jianjun Shi. Real-time monitoring of high-dimensional functional data streams via spatio-temporal smooth sparse decomposition. *Technometrics*, 60(2):181–197, 2018.
- [50] Steven A Yourstone and William J Zimmer. Non-normality and the design of control charts for averages. *Decision Sciences*, 23(5):1099–1113, 1992.

- [51] Chen Zhang, Nan Chen, and Jianguo Wu. Spatial rank-based high-dimensional monitoring through random projection. *Journal of Quality Technology*, 52(2):111–127, 2020.
- [52] Junjia Zhu and Dennis KJ Lin. Monitoring the slopes of linear profiles. *Quality Engineering*, 22(1):1–12, 2009.
- [53] Changliang Zou, Fugee Tsung, and Zhaojun Wang. Monitoring general linear profiles using multivariate exponentially weighted moving average schemes. *Technometrics*, 49(4):395–408, 2007.

A. The overlapping weighted CvM estimator

Algorithm 3 The overlapping weighted CvM estimator

Input: In-control monitoring statistics $\{T_t : t = 1, \dots, n\}$, batch size m .

- 1: For $i = 1, \dots, n - m + 1$, calculate

$$C_i = \frac{1}{m} \sum_{j=1}^m g\left(\frac{j}{m}\right) \frac{j^2}{m} (\bar{T}_{i,j} - \bar{T}_i)^2,$$

where the function $g(t) = -24 + 150t - 150t^2$, the partial batch mean $\bar{T}_{i,j} = \frac{1}{j} \sum_{j'=1}^j T_{i+j'}$ and the batch mean $\bar{T}_i = \frac{1}{m} \sum_{j=1}^m T_{i+j}$.

- 2: The CvM estimator is the average over all CvM estimators from the batches, namely

$$\Omega_0^2 = \frac{1}{n - m + 1} \sum_{i=1}^{n-m+1} C_i.$$

The CvM estimator is proposed by [2]. An expedient strategy for determining the batch size m could ensure the approximate independence among the batch means. Any applicable statistical test for independence can be employed for this purpose.

B. Proofs

Proof of Theorem 4.4. We begin by studying the statistical behaviors of in-control and out-of-control $\gamma_{i,t}$ separately.

- For the in-control case, Lemma 4.2 implies that $\gamma_{i,t} = o(\sqrt{p_1 p_2})$ almost surely.
- For an out-of-control case, Lemma 4.3 implies

$$\gamma_{i,t} = \sqrt{p_1 p_2} \bar{\rho}_i + z_i + o(\sqrt{p_1 p_2}) + o_p(1),$$

where $o_p(1)$ represents a random variable Z satisfying $\lim_{p_1, p_2 \rightarrow \infty} \mathbb{P}(|Z| \geq \epsilon) = 0$ for any positive constant ϵ . Then, we have

$$\frac{\mathbb{E}_1[\gamma_{i,t}] - \mathbb{E}_0[\gamma_{i,t}]}{\sqrt{p_1 p_2}} = \bar{\rho}_i + o(1).$$

□

Proof of Theorem 4.5. Without specifying the probability measure, we can decompose T_t into the following components.

$$\begin{aligned} \mathbb{E}_v[T_t] &= \mathbb{E}_v \left[(y_t - \mathbb{E}_0[y_t])^\top \text{Cov}_0^{-1}(y_t) (y_t - \mathbb{E}_0[y_t]) \right] \\ &= \mathbb{E}_v \left[(y_t - \mathbb{E}_v[y_t] + \mathbb{E}_v[y_t] - \mathbb{E}_0[y_t])^\top \text{Cov}_0^{-1}(y_t) (y_t - \mathbb{E}_v[y_t] + \mathbb{E}_v[y_t] - \mathbb{E}_0[y_t]) \right] \\ &= \text{tr}(\text{Cov}_0^{-1}(y_t) \text{Cov}_v^{-1}(y_t)) + (\mathbb{E}_v[y_t] - \mathbb{E}_0[y_t])^\top \text{Cov}_0^{-1}(y_t) (\mathbb{E}_v[y_t] - \mathbb{E}_0[y_t]), \quad v = 0, 1. \end{aligned}$$

Now we examine the difference between the in-control and out-of-control expectations:

$$\begin{aligned} \mathbb{E}_1[T_t] - \mathbb{E}_0[T_t] &= \text{tr}(\text{Cov}_0^{-1}(y_t) \text{Cov}_1^{-1}(y_t)) \\ &\quad + (\mathbb{E}_1[y_t] - \mathbb{E}_0[y_t])^\top \text{Cov}_0^{-1}(y_t) (\mathbb{E}_1[y_t] - \mathbb{E}_0[y_t]) - 2r \\ &= \text{tr}(\Sigma^{-1} \tilde{\Sigma}) + \delta^\top \Sigma^{-1} \delta - 2r. \end{aligned}$$

By utilizing the property of the Schur complement, we can express the inverse of Σ in the following form:

$$\Sigma^{-1} = \begin{bmatrix} \Sigma_\beta^{-1} + \Sigma_\beta^{-1} P (\Sigma/\Sigma_\beta)^{-1} P^\top \Sigma_\beta^{-1} & -\Sigma_\beta^{-1} P (\Sigma/\Sigma_\beta)^{-1} \\ -(\Sigma/\Sigma_\beta)^{-1} P^\top \Sigma_\beta^{-1} & (\Sigma/\Sigma_\beta)^{-1} \end{bmatrix},$$

where $\Sigma/\Sigma_\beta = \Sigma_\gamma - P^\top \Sigma_\beta^{-1} P$ denotes the Schur complement of the block Σ_β within the matrix Σ .

For $\text{tr}(\Sigma^{-1} \tilde{\Sigma})$, we have

$$\begin{aligned} \Sigma^{-1} \tilde{\Sigma} &= \begin{bmatrix} \Sigma_\beta^{-1} + \Sigma_\beta^{-1} P (\Sigma/\Sigma_\beta)^{-1} P^\top \Sigma_\beta^{-1} & -\Sigma_\beta^{-1} P (\Sigma/\Sigma_\beta)^{-1} \\ -(\Sigma/\Sigma_\beta)^{-1} P^\top \Sigma_\beta^{-1} & (\Sigma/\Sigma_\beta)^{-1} \end{bmatrix} \begin{bmatrix} \Sigma_\beta & \tilde{P} \\ \tilde{P}^\top & \tilde{\Sigma}_\gamma \end{bmatrix} \\ &= \begin{bmatrix} I_r + \Sigma_\beta^{-1} P (\Sigma/\Sigma_\beta)^{-1} P^\top - \Sigma_\beta^{-1} P (\Sigma/\Sigma_\beta)^{-1} \tilde{P}^\top & \left(\Sigma_\beta^{-1} + \Sigma_\beta^{-1} P (\Sigma/\Sigma_\beta)^{-1} P^\top \Sigma_\beta^{-1} \right) \tilde{P} - \Sigma_\beta^{-1} P (\Sigma/\Sigma_\beta)^{-1} \tilde{\Sigma}_\gamma \\ -(\Sigma/\Sigma_\beta)^{-1} P^\top + (\Sigma/\Sigma_\beta)^{-1} \tilde{P}^\top & -(\Sigma/\Sigma_\beta)^{-1} P^\top \Sigma_\beta^{-1} \tilde{P} + (\Sigma/\Sigma_\beta)^{-1} \tilde{\Sigma}_\gamma \end{bmatrix}. \end{aligned}$$

Then, its trace becomes

$$\begin{aligned}
& \text{tr}(\Sigma^{-1}\tilde{\Sigma}) \\
&= r + \text{tr} \left(\Sigma_{\beta}^{-1}P(\Sigma/\Sigma_{\beta})^{-1}P^{\top} - \Sigma_{\beta}^{-1}P(\Sigma/\Sigma_{\beta})^{-1}\tilde{P}^{\top} - (\Sigma/\Sigma_{\beta})^{-1}P^{\top}\Sigma_{\beta}^{-1}\tilde{P} + (\Sigma/\Sigma_{\beta})^{-1}\tilde{\Sigma}_{\gamma} \right) \\
&= r + \text{tr} \left[(\Sigma/\Sigma_{\beta})^{-1} \left(P^{\top}\Sigma_{\beta}^{-1}P - \tilde{P}^{\top}\Sigma_{\beta}^{-1}P - P^{\top}\Sigma_{\beta}^{-1}\tilde{P} + \tilde{\Sigma}_{\gamma} \right) \right] \\
&= r + \text{tr} \left[(\Sigma/\Sigma_{\beta})^{-1} \left(P^{\top}\Sigma_{\beta}^{-1}P - \tilde{P}^{\top}\Sigma_{\beta}^{-1}P - P^{\top}\Sigma_{\beta}^{-1}\tilde{P} + \tilde{P}^{\top}\Sigma_{\beta}^{-1}\tilde{P} - \tilde{P}^{\top}\Sigma_{\beta}^{-1}\tilde{P} + \tilde{\Sigma}_{\gamma} \right) \right] \\
&= r + \text{tr} \left\{ (\Sigma/\Sigma_{\beta})^{-1} \left\{ \left[\Sigma_{\beta}^{-1/2} (P - \tilde{P}) \right]^{\top} \left[\Sigma_{\beta}^{-1/2} (P - \tilde{P}) \right] + \tilde{\Sigma}/\Sigma_{\beta} \right\} \right\} \\
&= r + \text{tr} \left\{ (\Sigma/\Sigma_{\beta})^{-1} \left[\Sigma_{\beta}^{-1/2} (P - \tilde{P}) \right]^{\top} \left[\Sigma_{\beta}^{-1/2} (P - \tilde{P}) \right] \right\} + \text{tr} \left[(\Sigma/\Sigma_{\beta})^{-1} (\tilde{\Sigma}/\Sigma_{\beta}) \right],
\end{aligned}$$

where $\tilde{\Sigma}/\Sigma_{\beta} = \tilde{\Sigma}_{\gamma} - \tilde{P}^{\top}\Sigma_{\beta}^{-1}\tilde{P}$. For $\delta^{\top}\Sigma^{-1}\delta$, we have

$$\begin{aligned}
& \delta^{\top}\Sigma^{-1}\delta \\
&= \begin{bmatrix} \delta_{\beta}^{\top} & \delta_{\gamma}^{\top} \end{bmatrix} \begin{bmatrix} \Sigma_{\beta}^{-1} + \Sigma_{\beta}^{-1}P(\Sigma/\Sigma_{\beta})^{-1}P^{\top}\Sigma_{\beta}^{-1} & -\Sigma_{\beta}^{-1}P(\Sigma/\Sigma_{\beta})^{-1} \\ -(\Sigma/\Sigma_{\beta})^{-1}P^{\top}\Sigma_{\beta}^{-1} & (\Sigma/\Sigma_{\beta})^{-1} \end{bmatrix} \begin{bmatrix} \delta_{\beta} \\ \delta_{\gamma} \end{bmatrix} \\
&= \delta_{\beta}^{\top} \left[\Sigma_{\beta}^{-1} + \Sigma_{\beta}^{-1}P(\Sigma/\Sigma_{\beta})^{-1}P^{\top}\Sigma_{\beta}^{-1} \right] \delta_{\beta} \\
&\quad - \delta_{\beta}^{\top}\Sigma_{\beta}^{-1}P(\Sigma/\Sigma_{\beta})^{-1}\delta_{\gamma} - \delta_{\gamma}^{\top}(\Sigma/\Sigma_{\beta})^{-1}P^{\top}\Sigma_{\beta}^{-1}\delta_{\beta} + \delta_{\gamma}^{\top}(\Sigma/\Sigma_{\beta})^{-1}\delta_{\gamma} \\
&= \left\| \Sigma_{\beta}^{-1/2}\delta_{\beta} \right\|^2 + \left\| (\Sigma/\Sigma_{\beta})^{-1/2} \left(P^{\top}\Sigma_{\beta}^{-1}\delta_{\beta} + \delta_{\gamma} \right) \right\|^2.
\end{aligned}$$

Now, we substitute $\text{tr}(\Sigma^{-1}\tilde{\Sigma})$ and $\delta^{\top}\Sigma^{-1}\delta$ back into the expression for the shift size of T_t . Finally, we have

$$\begin{aligned}
& \mathbb{E}_1[T_t] - \mathbb{E}_0[T_t] \\
&= \text{tr}(\Sigma^{-1}\tilde{\Sigma}) + \delta^{\top}\Sigma^{-1}\delta - 2r \\
&= \text{tr} \left[(\Sigma/\Sigma_{\beta})^{-1} (\tilde{\Sigma}/\Sigma_{\beta}) \right] - r + \text{tr} \left\{ (\Sigma/\Sigma_{\beta})^{-1} \left[\Sigma_{\beta}^{-1/2} (P - \tilde{P}) \right]^{\top} \left[\Sigma_{\beta}^{-1/2} (P - \tilde{P}) \right] \right\} \\
&\quad + \left\| \Sigma_{\beta}^{-1/2}\delta_{\beta} \right\|^2 + \left\| (\Sigma/\Sigma_{\beta})^{-1/2} \left(P^{\top}\Sigma_{\beta}^{-1}\delta_{\beta} + \delta_{\gamma} \right) \right\|^2.
\end{aligned}$$

□